catalysts

MDPI

Article

Sepiolite-Supported WS_2 Nanosheets for Synergistically Promoting Photocatalytic Rhodamine B Degradation

Jiaxuan Bai [1,2], Kaibin Cui [1,2], Xinlei Xie [1,2], Baizeng Fang [3,*] and Fei Wang [1,2,*]

1 Key Laboratory of Special Functional Materials for Ecological Environment and Information, Ministry of Education, Hebei University of Technology, Tianjin 300130, China
2 Institute of Power Source and Ecomaterials Science, Hebei University of Technology, Tianjin 300130, China
3 Department of Chemical & Biological Engineering, University of British Columbia, 2360 East Mall, Vancouver, BC V6T 1Z3, Canada
* Correspondence: baizengfang@163.com (B.F.); wangfei@hebut.edu.cn (F.W.)

Abstract: Pristine tungsten disulfide (WS_2) nanosheets are extremely prone to agglomeration, leading to blocked active sites and the decrease of catalytic activity. In this work, highly dispersed WS_2 nanosheets were fabricated via a one-step in situ solvothermal method, using sepiolite nanofibers as a functional carrier. The ammonium tetrathiotungstate was adopted as W and S precursors, and *N*,*N*-dimethylformamide could provide a neutral reaction environment. The electron microscope analysis revealed that the WS_2 nanosheets were stacked compactly in the shape of irregular plates, while they were uniformly grown on the surface of sepiolite nanofibers. Meanwhile, the BET measurement confirmed that the as-prepared composite has a larger specific surface area and is more mesoporous than the pure WS_2. Due to the improved dispersion of WS_2 and the synergistic effect between WS_2 and the mesoporous sepiolite mineral which significantly facilitated the mass transport, the WS_2/sepiolite composite exhibited ca. 2.6 times the photocatalytic efficiency of the pure WS_2 for rhodamine B degradation. This work provides a potential method for low-cost batch preparation of high-quality 2D materials via assembling on natural materials.

Keywords: photocatalysis; rhodamine B degradation; sepiolite nanofibers; catalyst support; WS_2 nanosheets

Citation: Bai, J.; Cui, K.; Xie, X.; Fang, B.; Wang, F. Sepiolite-Supported WS_2 Nanosheets for Synergistically Promoting Photocatalytic Rhodamine B Degradation. *Catalysts* **2022**, *12*, 1400. https://doi.org/10.3390/catal12111400

Academic Editors: Gassan Hodaifa, Rafael Borja and Mha Albqmi

Received: 28 September 2022
Accepted: 3 November 2022
Published: 9 November 2022

1. Introduction

Since the last century, the environmental pollution caused by excessive discharge of organic pollutants in wastewater has led to the inadequacy of freshwater resources and threatened human health [1,2]. To solve these issues, photocatalysis could be regarded as a green and economical method. In fact, the rapid recombination rate of photogenerated electron-hole pairs and low solar light energy utilization efficiency significantly reduced the photocatalytic efficiency [3]. Compared with the prior photocatalysts containing ZnO and CdS, transition metal dichalcogenides (TMDCs) have received substantial interest due to their sandwich-like layered structure, strong photocatalytic activities, and favorable optical and electronic properties. WS_2 as a typical TMDC has been studied deeply due to its suitable bandgap, excellent stability, and nontoxic features [4,5]. However, pristine WS_2 has high specific surface energy and poor dispersion, and the spontaneous agglomeration of WS_2 with high specific surface energy always leads to a decrease in exposed active sites, which causes an unsatisfactory photocatalytic degradation effect. Thus, there has been little study on photocatalytic degradation of organic wastewater by pure WS_2, which has seriously hindered its practical application.

Fortunately, the development of supported WS_2 photocatalysts has become a feasible and promising approach. The active components dispersed on the surface of the support could increase the specific surface area and improve the catalytic efficiency of the active components per unit mass. A series of materials were combined with pure WS_2 to improve the photocatalytic performance. In previous reports, many carriers have been adopted to

support WS_2, such as graphene [6], reduced graphene oxide [7], TiO_2 [8], CdS [9], ZnO [10], Bi_2MoO_6 [11], etc. However, the high fabrication cost and complex process made these carriers unsuitable for broad applications. Natural minerals have the advantages of low cost, environmental friendliness, special morphology, and unique properties, which make them a very promising candidate for carriers. To date, different mineral-based composites with highly dispersed active compounds have been successfully synthesized.

Mineral materials are widely available and have been reported as catalyst carriers. Sepiolite (Sep) is a kind of natural magnesium silicate clay mineral, which is abundant in nature. Ascribed to the 1D fibrous structure, it has a strong adsorption capacity and high specific surface area [12–15]. As a carrier, sepiolite can improve the dispersion of materials. In addition, the interface effect between sepiolite and the loaded material can also enhance the photocatalytic performance. Sep has attracted much attention in the field of adsorbent and functional carrier for wastewater treatment [16–19].

In our previous studies, we have successfully synthesized ultrathin MoS_2 nanosheets with the assistance of sepiolite and tourmaline [20,21]. Herein, a novel WS_2/Sep composite with few layered WS_2 nanosheets was fabricated via an environmentally friendly and simple solvothermal route. The ultrathin WS_2 nanosheets that uniformly grow on the surface of the Sep led to the exposure of more surface-active sites and the solution to agglomeration. Furthermore, the WS_2/Sep composite exhibited much higher photocatalytic efficiency toward rhodamine B (RhB) degradation than the pristine WS_2, and the synergistic effect between WS_2 and Sep was also noted. This work offers a new insight for low-cost preparation of dispersed 2D material using natural minerals.

2. Results and Discussion

2.1. Crystal Phase and Groups Analysis

XRD patterns were recorded to examine the phase of the prepared pure WS_2 and WS_2/Sep composite (Figure 1a). All of the diffraction peaks of both the pure WS_2 nanosheets and WS_2/Sep composite matched well with the 2H hexagonal phase (JCPDS Card No.87-2417) [22]. The XRD patterns showed that the main peaks of WS_2 of the WS_2/Sep were located at 2θ = 13.775°, 28.6989°, 34.248°, and 47.105°, corresponding to the (002), (004), (101), and (103) facets of WS_2, and the diffraction peaks at 7.423°, 11.982°, 20.785°, and 26.667° corresponded well to the (011), (031), (131), and (080) facets of the Sep, respectively. The d-spacing value of the composite corresponding to the peak at 13.775° was calculated to be 6.4 Å, which was close to that of the pure WS_2. The few broad bread-like peaks could be attributed to the partial crystallization of the WS_2 nanosheets. After the solvothermal treatment, WS_2 was evenly dispersed on the support, and the diffraction peaks corresponding to WS_2 were sharp and symmetric, further confirming the great crystallization of composite. Furthermore, the FT-IR was used to identify the functional groups of the WS_2/Sep sample (Figure 1b). The broad absorption peaks at around 3567 cm^{-1} and 1652 cm^{-1} were ascribed to the stretching vibration of the hydroxyl group of crystal water. The peaks at 1003, 975, 424, and 788 cm^{-1} were ascribed to the stretching of the Si-O band in the Si-O-Si groups of sepiolite. The peaks at 669, 688, and 645 cm^{-1} corresponded to the bending vibration of Mg_3OH. The peaks at 464 were attributed to Si-O-Al (octahedral) and Si-O-Si [23–25]. The two intensive peaks at around 2358 and 2119 cm^{-1} originated from the characteristic peaks of hexagonal WS_2. The results of XRD and FT-IR revealed the WS_2/Sep maintained the original crystal structure and surface functional groups of WS_2 and sepiolite.

2.2. Morphology and EDS Analysis

SEM, TEM, and HRTEM were used to observe the microstructure of the pure WS_2 and WS_2/Sep (Figure 2). The pure WS_2 with the shape of irregular plates consisted of WS_2 nanosheets stacked compactly (Figure 2a). In Figure 2b, one can observe the WS_2 nanosheets were uniformly anchored on the surface of Sep nanofibers, and a bark-like structure was formed intimately; the WS_2 nanosheets in the WS_2/Sep composite owned better dispersion. Compared with the pure WS_2 nanosheets, the mineral material (i.e., Sep)

as a support of the composite could significantly reduce the agglomeration of the WS_2 nanosheets. Thus, more surface active sites of WS_2 could be exposed outside. The above results provided direct evidence that the WS_2 phase had been uniformly loaded on the Sep nanofibers.

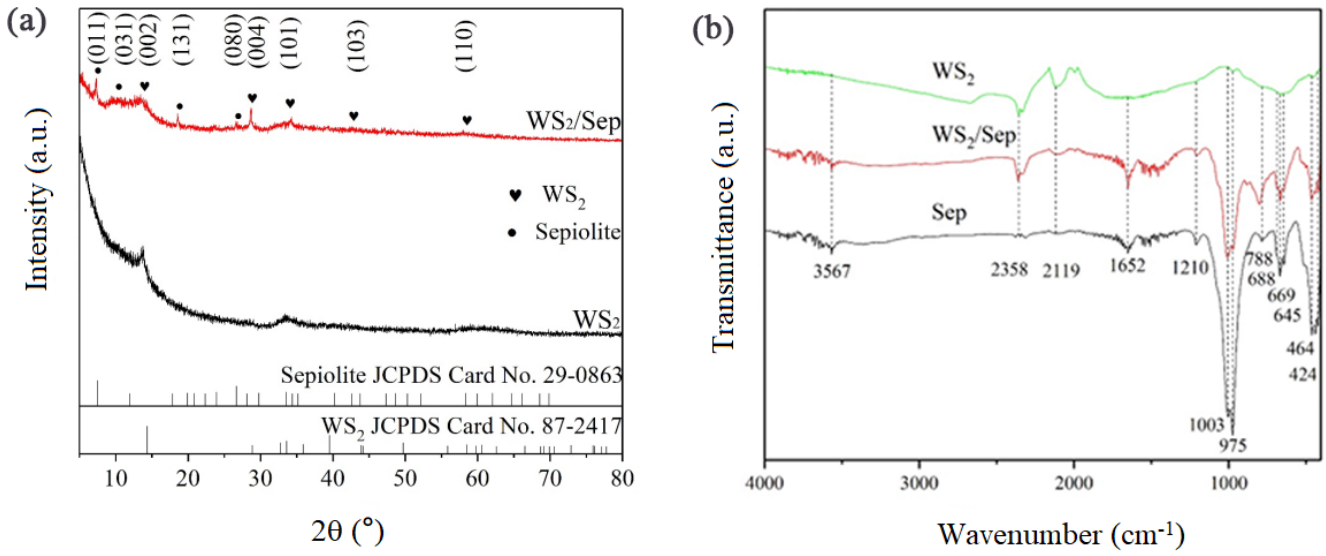

Figure 1. (**a**) XRD patterns of the pure WS_2 and WS_2/Sep nanocomposites obtained via solvothermal at 220 °C (**b**) and FT-IR spectra of the pure WS_2, sepiolite, and WS_2/Sep nanocomposites.

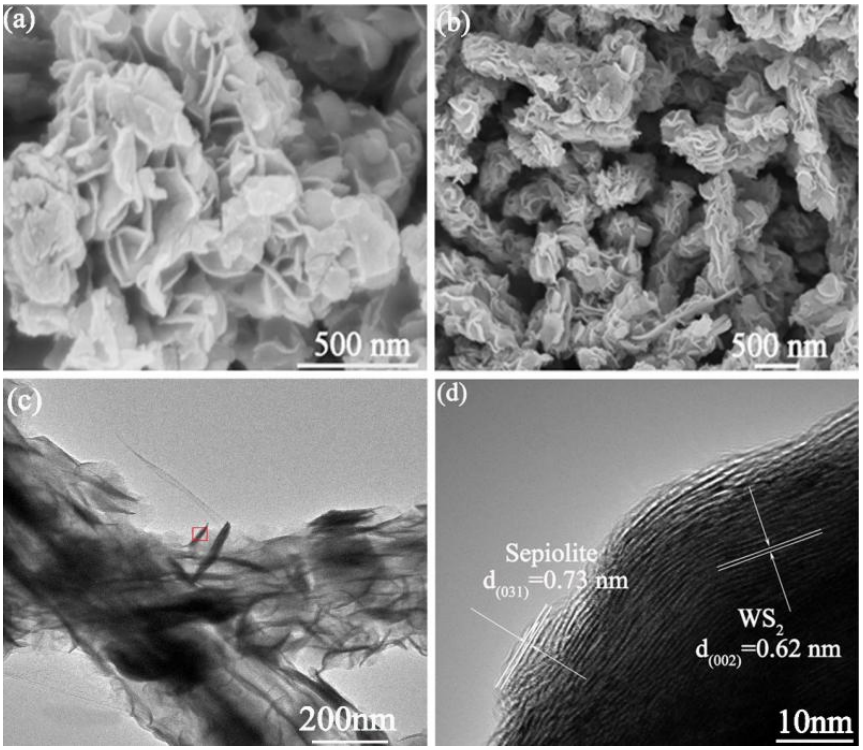

Figure 2. Morphology and structure of the pure WS_2 and WS_2/sepiolite nanocomposite. (**a**,**b**) SEM images of the pure WS_2 and WS_2/sepiolite nanocomposite obtained via solvothermal; (**c**,**d**) TEM and HRTEM images of WS_2/Sep.

TEM and HRTEM observations were adopted to deeply investigate the microstructure of the WS_2/Sep composite (Figure 2c,d), which further illustrated that the WS_2 phase had been loaded successfully on the surface of the Sep nanofibers. Moreover, the HRTEM

images (Figure 2d) indicated a lattice space distance of 0.62 nm, which corresponded to the (002) facet of 2H-WS_2 [26,27]. Lattice spacing consistent with the d-spacing of Sep (031) was also detected. In addition, the elemental mapping images (Figure 3) also confirmed that WS_2 nanosheets were successfully assembled on the surface of Sep mineral.

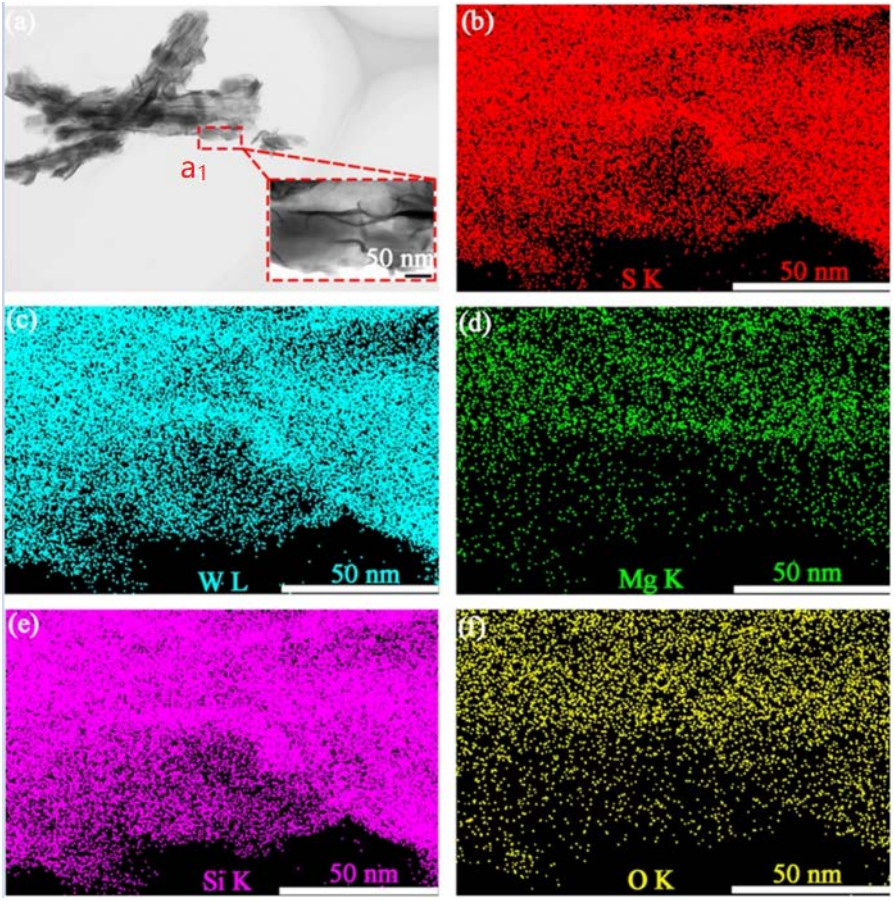

Figure 3. EDS mapping analysis of element distribution (**b**–**f**) in marked area (red rectangle in (**a**)) for the WS_2/Sep nanocomposite: S (**b**), W (**c**), Mg (**d**), Si (**e**), and O (**f**).

2.3. Nitrogen Adsorption-Desorption Analysis

Nitrogen adsorption-desorption isotherms and pore size distribution curves were adopted to further compare the surface area and pore structure between the WS_2/Sep composite and pure WS_2 (Figure 4). Both the samples presented Langmuir type IV isotherms with H3 hysteresis type loops, suggesting the existence of slit-like mesoporous structures because of the stacking of sheets. This was consistent with the electron microscopy images. The WS_2/Sep composite possessed a specific surface area of 45.9 m^2/g, which was much larger than that of the pure WS_2 (25.3 m^2/g). Meanwhile, the pore volume of the WS_2/Sep (0.107 cm^3/g) was also much larger than that of the WS_2 (0.048 cm^3/g). Consequently, the composite could expose more surface active sites and increase the number of mesopores, which tended toward improving catalytic activity [28].

2.4. Photocatalytic Performance of RhB Degradation

Comparative experiments were performed to evaluate the performance of the WS_2/Sep nanocomposite for RhB degradation, which is shown in Figure 5. It can be clearly seen that the WS_2/Sep composite exhibited much higher photocatalytic efficiency than the pure WS_2. After 150 min catalysis, the RhB degradation rate for the pure WS_2 only reached ~18%, while it achieved ca. 76% for the WS_2/Sep nanocomposites. The 4.2-fold improved activity could be mainly attributed to the better dispersion of the WS_2 nanosheets [20]. In

addition, the excellent synergies between the WS_2 nanosheets and Sep nanofibers could also accelerate the photocatalysis, which will be further discussed in the following section.

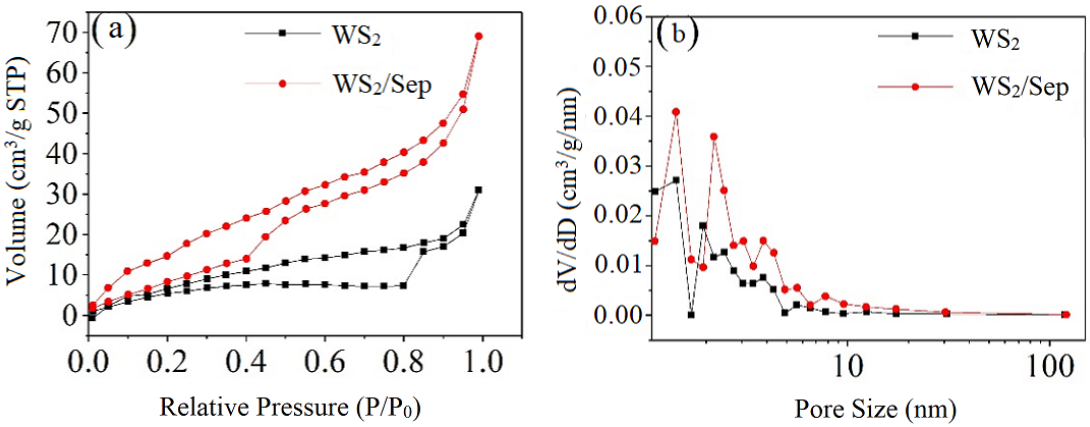

Figure 4. Nitrogen adsorption-desorption isotherms (**a**) and the corresponding pore size distribution curves (**b**) of WS_2 and WS_2/sepiolite composite.

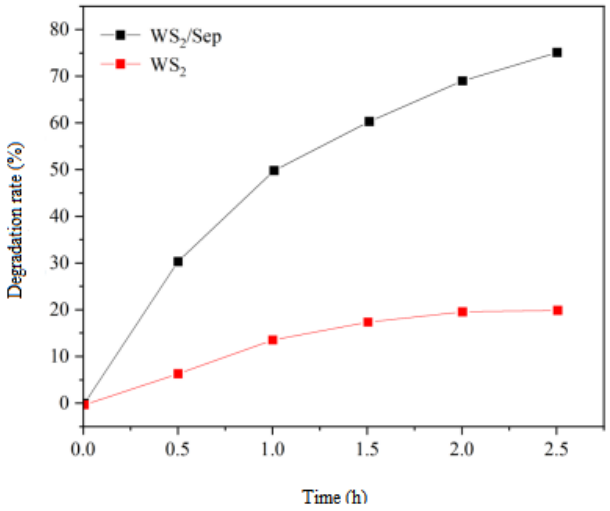

Figure 5. Photocatalytic activity of the WS_2/Sep composite and pure WS_2.

2.5. The Possible RhB Degradation Mechanism for the WS_2/Sep Composite

Figure 6 shows the possible process of the photocatalytic RhB degradation in which the synergic effect between the Sep and the grown WS_2 in the WS_2/sepiolite nanocomposite is illustrated. Under irradiation, the holes (h^+) and electrons (e^-) were produced. Then, the dissolved O_2 would react with e^- and OH− would react with h^+ to generate superoxide anion radical ($\cdot O_2^-$) and hydroxyl radical (·OH), respectively [29,30]. Finally, the RhB molecules adsorbed on the surface-active sites of the WS_2 were degraded to CO_2 and H_2O [31,32]. During this process, the excellent adsorption of Sep was conductive to transferring the dissolved O_2 and RhB molecules to the active sites of the WS_2, and the abundant hydroxyl (–OH) groups on the Sep surface also benefited the production of ·OH [33–35]. Thus, in addition to the improved dispersion of WS_2, the synergic effects provided by the Sep during photocatalysis also enabled the WS_2/Sep composite to exhibit much higher photocatalytic activity than the pure WS_2 [36]. Furthermore, the presence of mesopores favored multilight scattering, resulting in enhanced harvesting of the exciting light, and accordingly, improved photocatalytic activity [37,38]. These mesopores also facilitated fast mass transport and thus enhanced the performance [39,40].

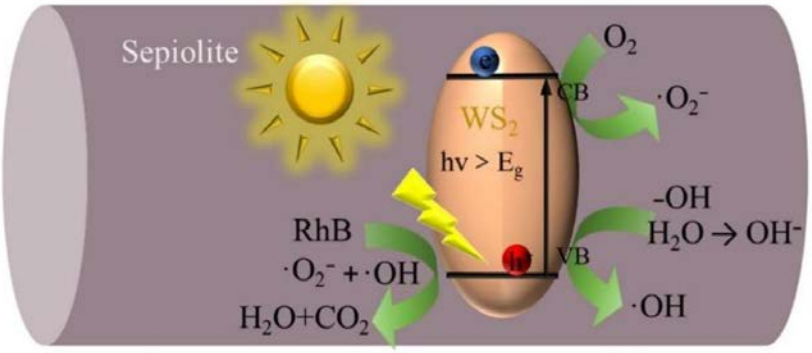

Figure 6. Possible RhB degradation mechanism of the WS_2/Sep composite.

3. Experiment

3.1. Chemicals and Reagents

The Sep was provided by LB Nanomaterials Technology Co., Ltd. (Henan, China), and the chemical analysis of the Sep was determined as SiO_2 of 53.56 wt%, MgO of 36.79 wt%, CaO of 5.53 wt%, Fe_2O_3 of 1.17 wt%, and other impurities of 2.95 wt%. The ammonium tetrathiotungstate ($H_8N_2S_4W$) and dimethylformamide (DMF) were supplied by Sigma-Aldrich Co., Ltd (Shanghai, China). The (RhB) was purchased from Kewei Chemical Group Co., Ltd. (Tianjin, China). All chemicals used in the experiments were of analytical grade. These materials were used without further purification. Deionized (DI) water was used in all experiments.

3.2. Synthesis of WS_2/Sep Nanocomposite

The WS_2/Sep nanocomposite was fabricated by a solvothermal method (Figure 7). A total of 30 mg of $H_8N_2S_4W$ was dissolved in 15 mL of *N*,*N*-dimethylformamide (DMF) and stirred for 0.5 h. Then, 10 mg of Sep powder was added into the solution and stirred continuously for 0.5 h. Next, the above mixture was sonicated for 10 min. Later, the above suspension was transferred into a 25 mL Teflon-sealed autoclave and heated to 220 °C for 24 h. After cooling down to room temperature, the final product was obtained by filtration, washed several times with DI water, and dried in a vacuum oven at 80 °C for 12 h. The preparation process of the pure WS_2 was similar to that of the WS_2/Sep nanocomposite but without the addition of Sep.

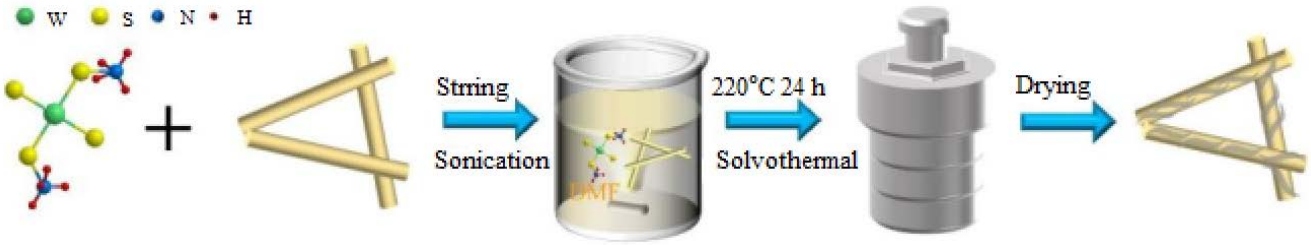

Figure 7. Schematic illustration for the synthesis process of WS_2/Sep composite.

3.3. Physicochemical Characterizations of the Synthesized WS_2/Sep Composite

X-ray powder diffraction (XRD) analysis was performed with the working conditions of Cu K_α radiation (λ = 1.54 Å), 40 mA, and 40 kV on a Smart Lab 9 KW X-ray diffractometer from Rigaku (Tokyo, Japan). Fourier-transform infrared spectroscopy (FTIR) spectra of the samples were recorded in a transmission mode from 400 to 4000 cm^{-1} on a Tensor II Fourier transform infrared spectrometer manufactured by Bruker (Saarbrucken, Germany). The morphologies of the as-synthesized samples were observed by using a S-4800 scanning electron microscope working at 5 kV, from JEOL (Tokyo, Japan). Transmission electron microscope (TEM) images, high-resolution TEM (HRTEM) images, and energy-dispersive

X-ray spectroscopy (EDS) were carried out on a JEM 2100F transmission electron microscope, from JEOL (Tokyo, Japan), with an accelerating voltage of 200 kV. The N_2 adsorption-desorption tests were conducted on Autosorb-iQ2, from Quantachrome (Boynton Beach, FL, USA). All samples were outgassed in nitrogen flow at 200 °C for 4 h before measurements. The specific surface area (SSA) was evaluated using the Brunauer-Emmett-Teller (BET) method, and the total pore volume was calculated at the relative pressure of approximately 0.99. The pore size distribution was computed using the Barrett-Joyner-Halenda (BJH) method.

3.4. Photocatalytic Performance Tests

Photocatalytic activity of the as-prepared samples was assessed by the reduction of RhB in aqueous solutions, using a 500 W Xe lamp equipped with a cut-off filter ($\lambda > 420$ nm). In a typical evaluation procedure, 20 mg of sample was added into 100 mL of RhB solution with a concentration of 20 mg/L at room temperature [41]. The suspension solution stirred vigorously in the dark for 0.5 h to reach the equilibrium of adsorption/desorption before visible light irradiation. At an interval of 0.5 h, 5.6 mL of the suspension was collected and centrifuged for absorbance analysis. The concentration of dye solution was analyzed by recording the UV–vis spectra at wavelength of 553 nm using a Shimadzu UV-1800 spectrophotometer from Shimadzu (Shimane, Japan).

4. Conclusions

In summary, a novel WS_2/Sep composite as a photocatalyst was successfully prepared via a facile solvothermal method. The physicochemical characterization results confirmed that the bark-like WS_2 nanosheets uniformly grew on the Sep nanofibers, which led to a larger surface area and more exposed active sites. In a typical photocatalytic application, the as-synthesized WS_2/Sep exhibited considerably improved photocatalytic performance for RhB degradation over the pure WS_2, which could be mainly attributed to the better dispersion of WS_2 nanosheets and the synergistic effect between the WS_2 nanosheets and the Sep nanofibers' support during the photocatalysis. This work is believed to provide new ideas for the low-cost batch preparation of high-quality two-dimensional materials based on natural minerals. However, further investigation of the as-developed composite photocatalyst with respect to reusability and the versatility for the degradation of other organic pollutants are still needed to see if there are any limitations to its practical applications.

Author Contributions: Conceptualization, F.W. and J.B.; methodology, F.W. and J.B.; software, J.B. and K.C.; validation, F.W. and J.B.; formal analysis, F.W. and J.B.; investigation, J.B. and K.C.; resources, F.W.; data curation, J.B. and F.W.; writing—original draft preparation, J.B.; K.C.; X.X., B.F.; and F.W.; writing—review and editing, F.W. and B.F.; visualization, F.W. and B.F.; supervision, F.W.; project administration, F.W.; funding acquisition, F.W. All authors have read and agreed to the published version of the manuscript.

Funding: This work was financially supported by the National Key R&D Program of China (No. 2021YFC1910605), the National Natural Science Foundation of China (No. 51874115), the Introduced Overseas Scholars Program of Hebei province, China (No. C201808), and the Excellent Young Scientist Foundation of Hebei province, China (No. E2018202241).

Data Availability Statement: Data will be available upon request from the corresponding authors.

Acknowledgments: Authors acknowledge the financial support by the National Key R&D Program of China (No. 2021YFC1910605), the National Natural Science Foundation of China (No. 51874115), the Introduced Overseas Scholars Program of Hebei province, China (No. C201808), and the Excellent Young Scientist Foundation of Hebei province, China (No. E2018202241).

Conflicts of Interest: The authors declare no conflict of interest.

References

1. Yahya, N.; Aziz, F.; Jamaludin, N.A.; Mutalib, M.A.; Ismail, A.F.; Salleh, W.N.W.; Jaafar, J.; Yusof, N.; Ludin, N.A. A review of integrated photocatalyst adsorbents for wastewater treatment. *J. Environ. Chem. Eng.* **2018**, *6*, 7411–7425. [CrossRef]
2. Yaqoob, A.A.; Parveen, T.; Umar, K.; Mohamad Ibrahim, M.N. Role of nanomaterials in the treatment of wastewater: A review. *Water* **2020**, *12*, 495. [CrossRef]
3. Liao, G.; Li, C.; Li, X.; Fang, B. Emerging polymeric carbon nitride Z-scheme systems for photocatalysis. *Cell Rep. Phys. Sci.* **2021**, *2*, 100355. [CrossRef]
4. Cong, C.; Shang, J.; Wang, Y.; Yu, T. Optical properties of 2D semiconductor WS_2. *Adv. Opt. Mater.* **2018**, *6*, 1700767. [CrossRef]
5. Manzeli, S.; Ovchinnikov, D.; Pasquier, D.; Yazyev, O.V.; Kis, A. 2D transition metal dichalcogenides. *Nat. Rev. Mater.* **2017**, *2*, 17033. [CrossRef]
6. Yuan, L.; Chung, T.F.; Kuc, A.; Wan, Y.; Xu, Y.; Chen, Y.P.; Heine, T.; Huang, L. Photocarrier generation from interlayer charge-transfer transitions in WS_2-graphene heterostructures. *Sci. Adv.* **2018**, *4*, e1700324. [CrossRef]
7. Wang, X.; Gu, D.; Li, X.; Lin, S.; Zhao, S.; Rumyantseva, M.; Gaskov, A. Reduced graphene oxide hybridized with WS_2 nanoflakes based heterojunctions for selective ammonia sensors at room temperature. *Sens. Actuators B Chem.* **2019**, *282*, 290–299. [CrossRef]
8. Lu, Z.; Cao, Z.; Hu, E.; Hu, K.; Hu, X. Preparation and tribological properties of WS_2 and WS_2/TiO_2 nanoparticles. *Tribol. Int.* **2019**, *130*, 308–316. [CrossRef]
9. Su, L.; Luo, L.; Song, H.; Wu, Z.; Tu, W.; Wang, Z.J.; Ye, J. Hemispherical shell-thin lamellar WS_2 porous structures composited with CdS photocatalysts for enhanced H_2 evolution. *Chem. Eng. J.* **2020**, *388*, 124346. [CrossRef]
10. Pataniya, P.M.; Late, D.; Sumesh, C.K. Photosensitive WS_2/ZnO nano-heterostructure-based electrocatalysts for hydrogen evolution reaction. *ACS Appl. Energy Mater.* **2021**, *4*, 755–762. [CrossRef]
11. Gao, J.; Liu, C.; Wang, F.; Jia, L.; Duan, K.; Liu, T. Facile synthesis of heterostructured WS_2/Bi_2MoO_6 as high-performance visible-light-driven photocatalysts. *Nanoscale Res. Lett.* **2017**, *12*, 377. [CrossRef] [PubMed]
12. Chen, Q.; Zhu, R.; Liu, S.; Wu, D.; Fu, H.; Zhu, J.; He, H. Self-templating synthesis of silicon nanorods from natural sepiolite for high-performance lithium-ion battery anodes. *J. Mater. Chem. A* **2018**, *6*, 6356–6362. [CrossRef]
13. Li, Z.; Gómez-Avilés, A.; Sellaoui, L.; Bedia, J.; Bonilla-Petriciolet, A.; Belver, C. Adsorption of ibuprofen on organo-sepiolite and on zeolite/sepiolite heterostructure: Synthesis, characterization and statistical physics modeling. *Chem. Eng. J.* **2019**, *371*, 868–875. [CrossRef]
14. Santos, S.C.R.; Boaventura, R.A.R. Adsorption of cationic and anionic azo dyes on sepiolite clay: Equilibrium and kinetic studies in batch mode. *J. Environ. Chem. Eng.* **2016**, *4*, 1473–1483. [CrossRef]
15. Zhang, J.; Yan, Z.; Ouyang, J.; Yang, H.; Chen, D. Highly dispersed sepiolite-based organic modified nanofibers for enhanced adsorption of Congo red. *Appl. Clay Sci.* **2018**, *157*, 76–85. [CrossRef]
16. Ma, Y.; Zhang, G. Sepiolite nanofiber-supported platinum nanoparticle catalysts toward the catalytic oxidation of formaldehyde at ambient temperature: Efficient and stable performance and mechanism. *Chem. Eng. J.* **2016**, *288*, 70–78. [CrossRef]
17. Selvitepe, N.; Balbay, A.; Saka, C. Optimisation of sepiolite clay with phosphoric acid treatment as support material for CoB catalyst and application to produce hydrogen from the $NaBH_4$ hydrolysis. *Int. J. Hydrogen Energy* **2019**, *44*, 16387–16399. [CrossRef]
18. Xu, X.; Chen, W.; Zong, S.; Ren, X.; Liu, D. Atrazine degradation using Fe_3O_4-sepiolite catalyzed persulfate: Reactivity, mechanism and stability. *J. Hazard. Mater.* **2019**, *377*, 62–69. [CrossRef]
19. Zhou, F.; Yan, C.; Sun, Q.; Komarneni, S. TiO_2/Sepiolite nanocomposites doped with rare earth ions: Preparation, characterization and visible light photocatalytic activity. *Micropor. Mesopor. Mater.* **2019**, *274*, 25–32. [CrossRef]
20. Wang, F.; Hao, M.; Liu, W.; Yan, P.; Fang, B.; Li, S.; Liang, J.; Zhu, M.; Cui, L. Low-cost fabrication of highly dispersed atomically-thin MoS_2 nanosheets with abundant active Mo-terminated edges. *Nano Mater. Sci.* **2021**, *3*, 205–212. [CrossRef]
21. Hao, M.; Li, H.; Cui, L.; Liu, W.; Fang, B.; Liang, J.; Xie, X.; Wang, D.; Wang, F. Higher photocatalytic removal of organic pollutants using pangolin-like composites made of 3–4 atomic layers of MoS_2 nanosheets deposited on tourmaline. *Environ. Chem. Lett.* **2021**, *19*, 3573–3582. [CrossRef]
22. Sun, Y.; Wu, J.; Zhang, L. Fabrication of Ag-WS_2 composites with preferentially oriented WS_2 and its anisotropic tribology behavior. *Mater. Lett.* **2020**, *260*, 126975. [CrossRef]
23. Arabkhani, P.; Javadian, H.; Asfaram, A.; Sadeghfar, F.; Sadegh, F. Synthesis of magnetic tungsten disulfide/carbon nanotubes nanocomposite (WS_2/Fe_3O_4/CNTs-NC) for highly efficient ultrasound-assisted rapid removal of amaranth and brilliant blue FCF hazardous dyes. *J. Hazard. Mater.* **2021**, *420*, 126644. [CrossRef] [PubMed]
24. Uğurlu, M.; Karaoğlu, M.H. TiO_2 supported on sepiolite: Preparation, structural and thermal characterization and catalytic behaviour in photocatalytic treatment of phenol and lignin from olive mill wastewater. *Chem. Eng. J.* **2011**, *166*, 859–867. [CrossRef]
25. Zhang, Y.; Wang, D.; Zhang, G. Photocatalytic degradation of organic contaminants by TiO_2/sepiolite composites prepared at low temperature. *Chem. Eng. J.* **2011**, *173*, 1–10. [CrossRef]
26. Anto Jeffery, A.; Nethravathi, C.; Rajamathi, M. Two-dimensional nanosheets and layered hybrids of MoS_2 and WS_2 through exfoliation of ammoniated MS_2 (M = Mo, W). *J. Phys. Chem. C* **2014**, *118*, 1386–1396. [CrossRef]

27. Yang, J.; Voiry, D.; Ahn, S.J.; Kang, D.; Kim, A.Y.; Chhowalla, M.; Shin, H.S. Two-dimensional hybrid nanosheets of tungsten disulfide and reduced graphene oxide as catalysts for enhanced hydrogen evolution. *Angew. Chem. Int. Ed.* **2013**, *52*, 13751–13754. [CrossRef]
28. Liu, C.; Chai, B.; Wang, C.; Yan, J.; Ren, Z. Solvothermal fabrication of MoS_2 anchored on $ZnIn_2S_4$ microspheres with boosted photocatalytic hydrogen evolution activity. *Int. J. Hydrogen Energy* **2018**, *43*, 6977–6986. [CrossRef]
29. Wu, Y.; Liu, Z.; Li, Y.; Chen, J.; Zhu, X.; Na, P. Construction of 2D-2D TiO_2 nanosheet/layered WS_2 heterojunctions with enhanced visible-light-responsive photocatalytic activity. *Chin. J. Catal.* **2019**, *40*, 60–69. [CrossRef]
30. Feng, Z.; Zeng, L.; Chen, Y.; Ma, Y.; Zhao, C.; Jin, R.; Lu, Y.; Wu, Y.; He, Y. In situ preparation of Z-scheme MoO_3/g-C_3N_4 composite with high performance in photocatalytic CO_2 reduction and RhB degradation. *J. Mater. Res.* **2017**, *32*, 3660–3668. [CrossRef]
31. Baral, A.; Das, D.; Minakshi, M.; Ghosh, M.; Padhi, D. Probing environmental remediation of RhB organic dye using α-MnO_2 under visible-light irradiation: Structural, photocatalytic and mineralization studies. *ChemistrySelect* **2016**, *1*, 4277–4285. [CrossRef]
32. Zhang, Q.; Tai, M.; Zhou, Y.; Zhou, Y.; Wei, Y.; Tan, C.; Wu, Z.; Li, J.; Lin, H. Enhanced Photocatalytic Property of γ-$CsPbI_3$ Perovskite Nanocrystals with WS_2. *ACS Sustain. Chem. Eng.* **2019**, *8*, 1219–1229. [CrossRef]
33. Elangovan, E.; Sivakumar, T.; Brindha, A.; Thamaraiselvi, K.; Sakthivel, K.; Kathiravan, K.; Aishwarya, S. Visible Active N-Doped TiO_2/WS_2 Heterojunction Nano Rods: Synthesis, Characterization and Photocatalytic Activity. *J. Nanosci. Nanotechnol.* **2019**, *19*, 4429–4437. [CrossRef] [PubMed]
34. Fu, S.; Yuan, W.; Liu, X.; Yan, Y.; Liu, H.; Li, L.; Zhao, F.; Zhou, J. A novel 0D/2D WS_2/BiOBr heterostructure with rich oxygen vacancies for enhanced broad-spectrum photocatalytic performance. *J. Colloid. Interface Sci.* **2020**, *569*, 150–163. [CrossRef]
35. Xiang, Q.; Cheng, F.; Lang, D. Hierarchical Layered WS_2/Graphene-Modified CdS Nanorods for Efficient Photocatalytic Hydrogen Evolution. *ChemSusChem* **2016**, *9*, 996–1002. [CrossRef] [PubMed]
36. Liu, X.; Xing, Z.; Zhang, Y.; Li, Z.; Wu, X.; Tan, S.; Yu, X.; Zhu, Q.; Zhou, W. Fabrication of 3D flower-like black N-TiO_{2-x}@MoS_2 for unprecedented-high visible-light-driven photocatalytic performance. *Appl. Catal. B Environ.* **2017**, *201*, 119–127. [CrossRef]
37. Liu, Y.; Shen, S.; Li, Z.; Ma, D.; Xu, G.; Fang, B. Mesoporous g-C_3N_4 nanosheets with improved photocatalytic performance for hydrogen evolution. *Mater. Charact.* **2021**, *174*, 111031. [CrossRef]
38. Liu, Y.; Xu, G.; Ma, D.; Li, Z.; Yan, Z.; Xu, A.; Zhong, W.; Fang, B. Synergistic effects of g-C_3N_4 three-dimensional inverse opals and Ag modification on high-efficiency photocatalytic H_2 evolution. *J. Clean. Prod.* **2021**, *328*, 129745. [CrossRef]
39. Fang, B.; Kim, J.; Kim, M.; Yu, J. Hierarchical nanostructured carbons with meso-macroporosity: Design, characterization and applications. *Acc. Chem. Res.* **2013**, *46*, 1397–1406. [CrossRef] [PubMed]
40. Fang, B.; Daniel, L.; Bonakdarpour, A.; Govindarajan, R.; Sharman, J.; Wilkinson, D. Dense Pt nanowire electrocatalysts for improved fuel cell performance using a graphitic carbon nitride-decorated hierarchical nanocarbon support. *Small* **2021**, *17*, 2102288. [CrossRef]
41. Ji, H.; Fei, T.; Zhang, L.; Yan, J.; Fan, Y.; Huang, J.; Song, Y.; Man, Y.; Tang, H.; Xu, H.; et al. Synergistic effects of MoO_2 nanosheets and graphene-like C_3N_4 for highly improved visible light photocatalytic activities. *Appl. Surf. Sci.* **2018**, *457*, 1142–1150. [CrossRef]